



Controlled synthesis of CuInS₂/reduced graphene oxide nanocomposites for efficient dye-sensitized solar cells



Lei Zhou ^a, Xiao Yang ^a, Bo Yang ^a, Xueqin Zuo ^a, Guang Li ^{a,b,*}, Ali Feng ^a, Huaibao Tang ^a, Haijun Zhang ^a, Mingzai Wu ^{a,b}, Yongqing Ma ^{a,b}, Shaowei Jin ^{a,b}, Zhaoqi Sun ^{a,b}, Xiaoshuang Chen ^c

^a School of Physics and Materials Science, Anhui University, Hefei 230601, China

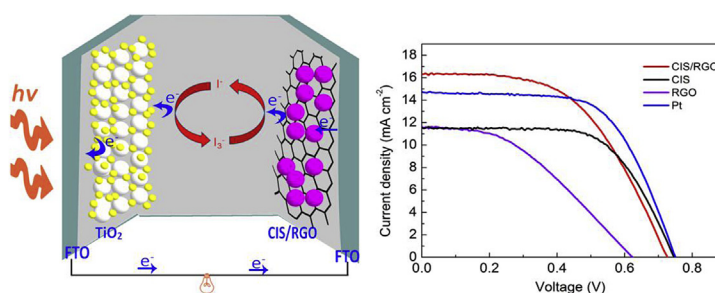
^b Anhui Key Laboratory of Information Materials and Devices, Hefei 230601, China

^c National Laboratory for Infrared Physics, Shanghai Institute of Technical Physics, Chinese Academy of Sciences, Shanghai 200083, China

HIGHLIGHTS

- CuInS₂ nanospheres are successfully grown on reduced graphene oxide layer.
- The nanocomposite has exhibited excellent electrocatalytic activity.
- A superior power conversion efficiency of 6.96% is achieved.

GRAPHICAL ABSTRACT



ARTICLE INFO

Article history:

Received 2 February 2014

Received in revised form

21 June 2014

Accepted 24 June 2014

Available online 10 September 2014

Keywords:

Nanocomposite

Controlled synthesis

Reduced graphene oxide

Dye-sensitized solar cells

ABSTRACT

A nanocomposite comprised CuInS₂ and reduced graphene oxide have been successfully synthesized via a facile two-step hydrothermal route using graphene oxide, thiourea, Indium chloride tetrahydrate and cuprous chloride as the raw materials, and L-Ascorbic acid as the reductant. Compared with pristine CuInS₂, CuInS₂ and reduced graphene oxide nanocomposites exploited as counter electrodes have exhibited outstanding electrocatalytic activity for the reduction of triiodide and excellent chemical stability due to the introduction of reduced graphene oxide. The characterization measurements indicate that the power conversion efficiency of dye-sensitized solar cell fabricated with CuInS₂ and reduced graphene oxide nanocomposites counter electrode achieves 6.96%, which is higher than that of device using pristine CuInS₂ counter electrode (5.49%), and comparable to the conventional platinum counter electrode (6.92%) under the same test conditions.

© 2014 Elsevier B.V. All rights reserved.

1. Introduction

As an optional effective alternative of silicon-based solar cell, dye-sensitized solar cells (DSSCs) have received numerous

attention of the academic and the commercial because of its low cost, long life, easy of fabrication and relatively high conversion efficiency. [1,2] Many efforts have been devoted to the development of DSSCs, and many significant breakthroughs have been created in the past few decades, especially this decade. [3–9] Recently, Simon Mathew and co-workers has reported the best power conversion efficiency (PCE) of 13%. [10] Generally, a typical DSSC is constituted with three main components: a

* Corresponding author. School of Physics and Materials Science, Anhui University, Hefei 230601, China. Tel.: +86 0551 63861867; fax: +86 0551 63861992.

E-mail address: liguang1971@ahu.edu.cn (G. Li).

porous structure oxide film, traditionally TiO_2 , as the photo-sensitized anode, a counter electrode (CE) as the catalytic cathode, and a liquid electrolyte traditionally containing an iodide/triiodide (I^-/I_3^-) redox couple between the two electrodes. Among them, CE collects electrons from the external circuit to catalyze the reduction of triiodide, which makes the whole circuit complete [11].

CE, as a considerably important component of DSSC, is always the object we concerned and researched. Usually, high electronic conductivity and superior electrocatalytic activity are the prerequisite to assess whether a CE material is excellent. Customarily, the CEs of DSSCs are thermally decomposed platinum (Pt) on fluorine-doped tin oxide (FTO) glass substrates owing to its remarkable electrocatalytic activity and excellent chemical stability. [12] However, relatively high cost and inferior resistance to corrosion in electrolyte have impeded the large-scale manufacture. Hence, the exploration of an appropriate alternative to noble metal Pt has been an urgent demand. In previous literature, many alternative materials have been exploited, such as conducting polymers, [13–15] carbon-based materials, [16–20] metallic nanomaterials, [21,22] nitrides, [23] sulfides, [24] oxides, [25] selenides, [26] and various hybrids. [27,28] Among them, sulfides obtain relatively more attention due to its mild conditions, such as lower temperatures, relatively facile preparation conditions and low toxicity. Some transition metal sulfides [29,30] which performed a comparable electrocatalytic activity to Pt have been reported. To our knowledge, much attention has been focused on binary compounds instead of multiple compounds in the past. Over the recent years, multimetal sulfides have gradually attracted particular attention due to their unique catalytic and electrical characteristics. The multimetal sulfide Xin et al. reported [31] exhibits excellent photovoltaic performance, even surpassing Pt CEs in DSSCs. The outstanding performance may originate from the synergistic mechanism of various metal elements. CuInS_2 (CIS), as a typical ternary metal sulfide, was explored as an absorber layer for high efficiency and radiation-hard solar cell application because of its high absorption coefficient and a relatively ideal direct band gap (1.5 eV). [32,33] In addition, recent works reveal that CIS have great potential as electrocatalytic material in DSSCs [29,30] due to its easy conversion of n/p carrier type, good stability under solar radiation and the ideal band gap which is close to the optimum range for high photovoltaic conversion. [32] Nevertheless, rare studies are centered on its electrocatalytic activity for use as CEs in DSSCs, to our knowledge. Therefore, we prepared a CIS nanomaterial as the CE for DSSCs. Considering the low charge mobility in CIS nanoparticles coming from the random boundaries between nanoparticles, a composite material of CIS with an excellent conductive material was produced to solve this drawback through the synergistic catalytic effect. In our work, we prepared a compound for DSSCs, which was few reported, [34] to the best of our knowledge.

Graphene, a potential atom-thick two-dimensional (2D) carbon material, has been researched in different fields in virtue of its outstanding electronic properties, excellent mechanical character, chemical inertness against corrosive electrolyte and ultra-large specific surface area. [35,36] Considering the inferior catalytic activity of pristine graphene CEs, we attempted to propose a nanocomposite of CuInS_2 nanoparticles with RGO (CIS/RGO) as the CEs of DSSCs. The immobilization of CIS onto RGO could dramatically improve the catalytic activity and therefore the photovoltaic performance due to the synergetic catalysis of CIS and RGO, which demonstrates that the compound of ternary metal sulfides with RGO is a feasible approach to enhance the performance of DSSCs.

2. Experimental details

2.1. Preparation of graphene oxide

Graphene oxide (GO) in our work was synthesized according to the improved Hummer's method. [37] Typically, the graphite flakes (300 mesh, 1.5 g) was added to a 9:1 mixture of concentrated $\text{H}_2\text{SO}_4/\text{H}_3\text{PO}_4$ (180:20 ml) under constant stirring. The reaction system was then heated to 50 °C followed by the slow addition of KMnO_4 , and stirred constantly for 6 h. Then, a large amount of distilled water (200 ml) with 30% H_2O_2 (1.5 ml) was slowly add to the reaction system until the mixture turn to bright yellow. Afterwards, the resulting suspension was filtered off and washed with 1:10 HCl solution (200 ml), distilled water and absolute alcohol successively until the pH value was close to 7. The obtained GO powder was dried in a vacuum oven overnight.

2.2. Preparation of CuInS_2 /RGO nanocomposites

A two-step approach was adopted in our work. In a typical synthesis process, 20, 40, 60, or 80 mg of GO powders and 3.0 mmol thiourea (Tu) were dispersed in 20 ml absolute alcohol, marked as solution A, and then treated by ultrasonication for 3 h in a beaker. Concomitantly, 1.0 mmol CuCl and 1.0 mmol $\text{InCl}_3 \cdot 4\text{H}_2\text{O}$ were dispersed in 20 ml absolute alcohol, followed by stirring for half an hour till homogeneous (solution B). Afterwards, solution A was added to solution B under stirring, and then continued to stir for 1 h. Then the mixture solution was transferred to a 50 ml Teflon-line stainless steel autoclave. The sealed autoclave was heated at 160 °C for 16 h and then cooled to room temperature. After that, 0.4 g of L-Ascorbic acid was added to the autoclave followed by stirring for 30 min and then hydrothermal reaction at 180 °C for another 8 h. After the reaction, the CuInS_2 nanospheres were formed on the surface of RGO. The precipitate was filtered, washed with absolute alcohol and distilled water for several times, and then dried in a vacuum oven at 60 °C for 12 h. The sample obtained from 40 mg of GO powders was chose to complete the experiment due to the most outstanding solar cell performance.

CuInS_2 was synthesized according to the same method in absence of GO, and RGO was prepared with the same method without the introduction of CuCl, $\text{InCl}_3 \cdot 4\text{H}_2\text{O}$ and thiourea, simultaneously.

2.3. Fabrication of counter electrodes

To prepare CEs, 0.1 g of RGO, CuInS_2 , and CuInS_2 /RGO were respectively mixed with Polyethylene glycol powder (0.025 g) and then dispersed into 5 ml ethanol followed by stirring to form a paste, typically. Afterwards, the paste was coated on FTO-coated glass (fluorine-doped tin oxide), which was masked by a 3 M Scotch tape with an exposed area of $0.5 \times 0.5 \text{ cm}^2$, via doctor-blading technique, and then dried to remove the solvent. Subsequently, the CEs were annealed at 450 °C for 1 h under the protection of argon atmosphere. As a comparison, commercial magnetron sputtering Pt CEs were purchased from Wuhan Georgi science instrument Co., Ltd (Wuhan, Hubei, China).

2.4. Assembly of DSSCs

Commercial TiO_2 photoanodes purchased from Dalian Hep-taChroma Solar Technology Development Co., Ltd (Dalian, Liaoning, China) were immersed in the N719 solution (0.3 mM in the solvent of ethanol) for 24 h. Whereafter, the dye-sensitized TiO_2 photoanodes were washed with anhydrous ethanol and dried in the flow of hot air. Finally, the TiO_2 photoanodes were assembled with the

as-prepared CEs with the injection of redox electrolyte (0.5 M LiI, 0.6 M 1-propyl-2, 3-dimethylimidazolium iodide, 0.05 M I_2 , and 0.5 M 4-tert-butylpyridine with acetonitrile as the solvent).

2.5. Characterization and photoelectrical measurements

The as-prepared samples were characterized on an X-ray powder diffraction (XRD) equipped with monochromatized Cu K α radiation ($\lambda = 1.5406 \text{ \AA}$) at 36 KV and 25 mA. The sizes and morphologies of CIS/RGO were investigated by high-resolution transmission electron microscopy (HRTEM; JEM-2100, JEOL, Japan) equipped with energy dispersive spectroscopy (EDS) and scanning electron microscopy (SEM; S-4800, Hitachi, Japan). The Raman scattering spectra were carried on a laser confocal micro Raman spectrometer (Invia-Reflex, Renishaw, UK) at 534 nm with a $100\times$ objective. Cyclic voltammetry (CV) was implemented on an electrochemical workstation (ZAHNER ZENNIUM CIMPS-1, Germany) with a three-electrode system (the prepared CEs as the working electrode, a symmetrical platinum sheets as the counter electrode, and saturated calomel electrode as the pseudoreference electrode) in an anhydrous acetonitrile solution of 0.1 M $LiClO_4$, 10 mM LiI, and 1 mM I_2 at a scan rate of 50 mV S^{-1} . Electrochemical impedance spectroscopy (EIS) were executed on dummy cells with a typical symmetric sandwich-like structure, that is, CE/electrolyte/CE, using an impedance measurement unit of workstation in the frequency range $0.1\text{--}10^6 \text{ Hz}$ with an ac amplitude of 10 mV. The photocurrent density-voltage (J-V) measurements were carried out on a Keithley 2410 digital source meter under AM 1.5 illumination (continuous solar simulator for PV cells, 100 mW cm^{-2}), which was calibrated by a Si reference cell beforehand. All the measurements were executed at room temperature.

3. Result and discussion

3.1. Compositions and morphology of CIS/RGO nanocomposites

The phase structure and crystallinity of CIS/RGO, CIS, RGO, and GO were typically characterized by the XRD patterns shown in Fig. 1. For GO, an evident characteristic peak were exhibited at $2\theta = 10.1^\circ$, corresponding to the (001) reflection and the interplanar spacing of 0.87 nm, [38] which indicated the well oxidation of graphite. In addition, no other obvious diffraction peak was observed suggesting that the imperfect graphene sheets remained disordered carbon structure and there were spaces between sheets. [39] Along with the reduction, this peak gradual broadened and receded to 23.6° for RGO, corresponding to an

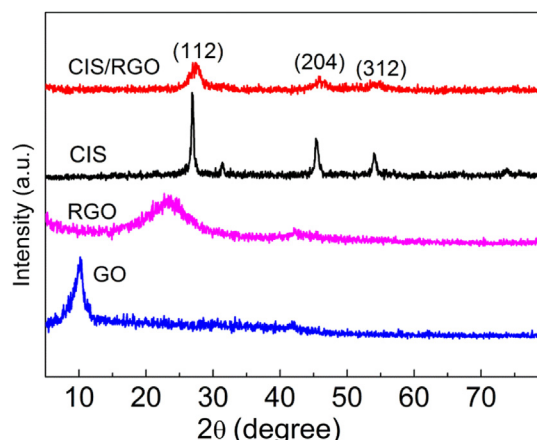


Fig. 1. XRD patterns of CIS/RGO, CIS, RGO and GO.

interplanar spacing of 0.37 nm, which indicated that the majority of the oxygen-containing functional groups were removed from GO. [40] For pristine CIS, all the diffraction peaks could be well indexed to chalcopyrite CIS (JCPDS card NO. 27-0159, $a = 5.523 \text{ \AA}$, $c = 11.14 \text{ \AA}$) with the lattice parameter of $a = 5.561 \text{ \AA}$, $c = 11.365 \text{ \AA}$. The diffraction peaks at 2θ of 27.9° , 46.2° and 55.1° could be assigned to (112), (204) and (312) planes of chalcopyrite CIS, respectively. The XRD pattern of CIS/RGO nanocomposite was consistent with pristine CIS, while diffraction peaks of RGO were not observed because the regular stack of RGO was destroyed by the intercalation of CIS nanoparticles, which weakened the diffraction intensity of RGO [41].

For the sake of further ascertaining the phase composition of the samples, Raman scattering spectra shown in Fig. 2 were conducted. For the pristine CIS, an obvious vibration band in $200\text{--}400 \text{ cm}^{-1}$ range is observed, which is consistent with the reported results of CIS. [42–44] As expected, the Raman spectrum of GO displays two prominent peaks at 1362 cm^{-1} and 1595 cm^{-1} , which are ascribed to the disordered (D) and graphitic (G) bands, respectively. [45] The spectrum of CIS/RGO exhibits three characteristic peaks, which are associated with CIS and GO, respectively. The D band and G band are slightly red-shifted to 1329 and 1574 cm^{-1} , which is attributed to the recovery of the hexagonal network of carbon atom. [46] The intensity ratio of D band and G band (I_D/I_G) generally indicates the degree of reduction of GO to graphene. The I_D/I_G is 0.91 for GO, which increases to 1.03 for RGO and 1.15 for CIS/RGO, confirming the well reduction of GO. The increased I_D/I_G can ascribe to the presence of unrepaired defects after the removal of partial oxygen moieties and the separation of graphene layer aroused by the intercalation of CIS nanoparticles. [47] In addition, the 2D band at ca. 2691 cm^{-1} and the D + G band at ca. 2927 cm^{-1} are magnified in the inset, which agrees with the previous literatures [48].

The morphology of CIS/RGO nanocomposites is depicted by SEM (Fig. 3) and TEM (Fig. 4). SEM images present that curled RGO sheets are decorated with CIS nanoparticles, which indicate a good loading of CIS nanoparticles. Fig. 3C–D shows the morphology of the prepared CIS/RGO CE after annealing. There are lots of cracks are observed on the surface of the CIS/RGO film, which may stem from the decomposition of Polyethylene glycol at high temperature. TEM images clearly exhibit that large quantity of CIS nanoparticles with an average particle diameter of about 100 nm are well attached on the graphene sheets. (Fig. 4a–c) However, the as-prepared pristine CIS via the same approach in absence of GO easily aggregate

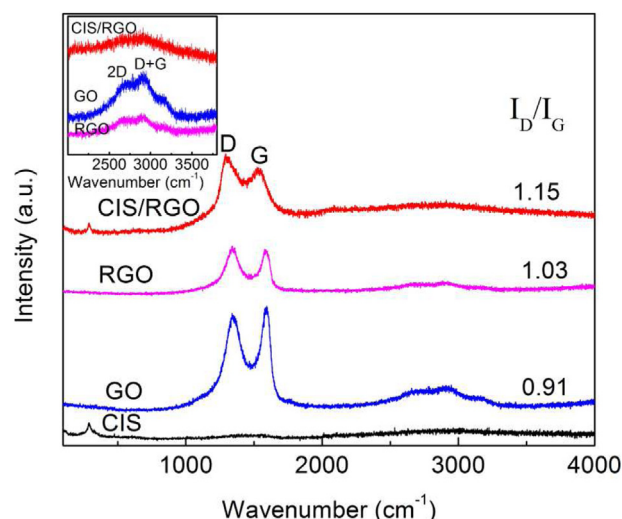


Fig. 2. Raman spectra of CIS/RGO, GO, and CIS.

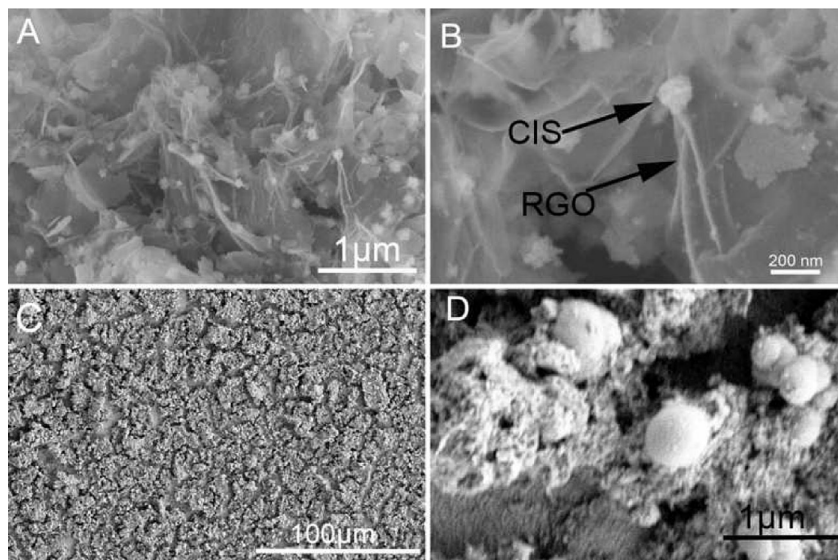


Fig. 3. FESEM images of CIS/RGO nanocomposites (A,B) and film (C,D) at low and high resolution.

together, which may illustrates that the GO sheets play an importance role in the well-dispersed growth on RGO sheets. In our present study, GO may provides a substrate for nucleation of CIS nanoparticles, and the deposition of CIS on RGO sheets helps to prevent the stack of the RGO sheets, confirming the interactions between graphene sheets and CIS nanoparticles. [41,49] Higher resolution transmission electron microscopy (HRTEM, Fig. 4d) reveals that the framework of CIS is monocrystalline and the interplanar spacing is about 3.195 Å, which corresponds to the (112) lattice plane spacing (JCPDS card NO. 27-0159, $d_{112} = 3.198$ Å). These indicate that the CIS/RGO samples have good crystallinity.

3.2. Formation mechanism

The formation process of the CIS/RGO nanocomposites is illustrated in Scheme 1. Previous literatures have proved that many

functional groups such as carboxyl, epoxy couple and hydroxyl existed on the basal plane and edge of GO nanosheets. The defect sites together with the negatively charged surface are favorable to capture cations. [50] Therefore, In^{3+} uniformly incorporates on GO sheets because of the electrostatic interaction. [51] CuCl in ethanol, practically insoluble, hardly provides Cu^+ at room temperature. At high temperature and vapor pressure, thiourea decomposes to yield S^{2-} , and CuCl slow releases Cu^+ , giving rise to the growth of CIS on the GO sheets. Ultimately, GO sheets are reduced to RGO sheets with the introduction of L-Ascorbic acid.

3.3. Photovoltaic behaviors of DSSCs

Fig. 5 depicts the J - V curves of DSSCs fabricated with CIS/RGO, CIS, RGO, and Pt CEs, and the detailed photovoltaic parameters are summarized in Table 1. The pristine CIS electrode gained a relatively

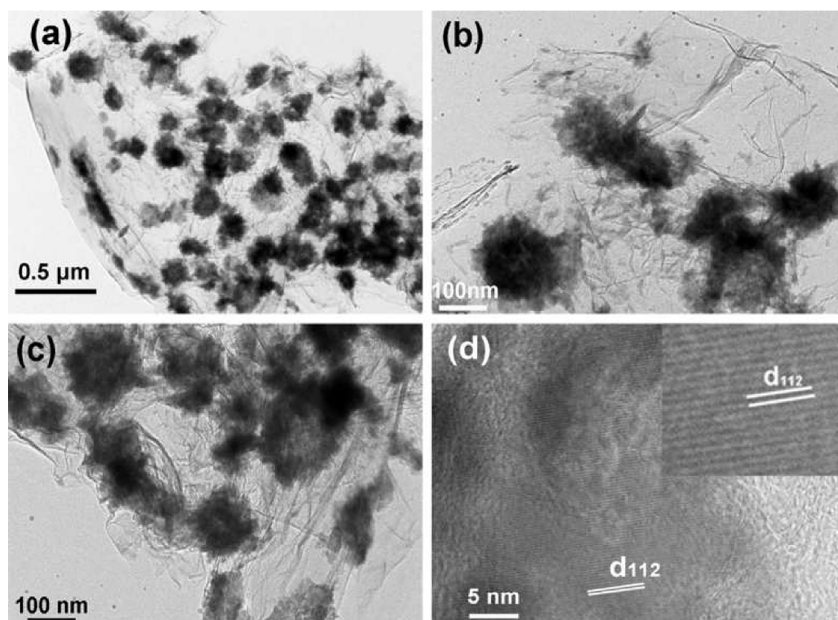
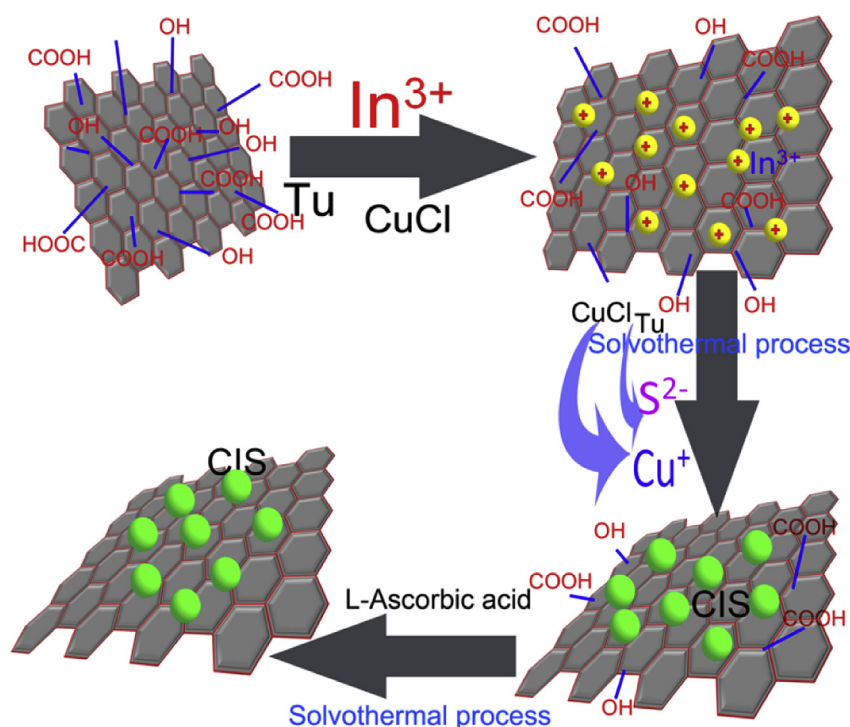


Fig. 4. TEM images (a, b, and c) and HRTEM image (d) of as-synthesized CIS/RGO.



Scheme 1. Schematic diagram of the synthetic route for CIS/RGO nanocomposites.

higher PCE (5.49%) than the DSSC with RGO electrode (2.79%), which mainly derives from the higher open-circuit photovoltage (V_{oc}) and filling factor (FF). In comparison, the CIS/RGO electrode exhibits a higher short-circuit current density (J_{sc}) of 16.61 mA cm^{-2} resulting in a higher PCE (6.96%), which is much higher than that of each component of the nanocomposites as the CEs. Compared to Pt electrode, the J_{sc} of CIS/RGO electrode is improved notably which are compensated by a somewhat low FF (57.56%) and V_{oc} (728 mV), and therefore yield a comparable efficiency to Pt. Interestingly, the largest FF is not that of Pt electrode (62.39%) or CIS/RGO electrode but CIS electrode (63.80%). We are unable to fully understand the aberrant result, and the difference between TiO_2 photoanode assembled with CIS and Pt CE may be a plausible cause because 62.39% is close to 63.80%. And the DSSC with CIS/RGO CE achieves a V_{oc} of 728 mV, which is lower than

pristine CIS (745 mV) and Pt (751 mV). These differences can be attributed to the higher proton concentration in the case of CIS and Pt, shifting the TiO_2 conduction band towards a more positive potential. [22] Meanwhile, the electrodes of different GO content ratio have already been prepared to conduct the experiments, which are marked in Fig. S1. The CIS/RGO sample obtained from 40 mg of GO powder exhibits the best solar cell performance compared to others. Distinctly, according to the increased content ratio of GO, J_{sc} and FF for samples with 40, 60, and 80 mg of GO powders gradually decline. The results suggest that the nanocomposite CEs can yield a comparable efficiency to that of Pt CE through adjusting the content ratio of each component.

3.4. Electrochemical properties of CEs

To investigate the catalytic activities of various CEs, cyclic voltammetry (CV, Fig. 6) was conducted in a three electrode system with the Pt sheet as CE, various CEs as WE (working electrode) and saturated calomel electrode as RE (reference electrode). Typically,

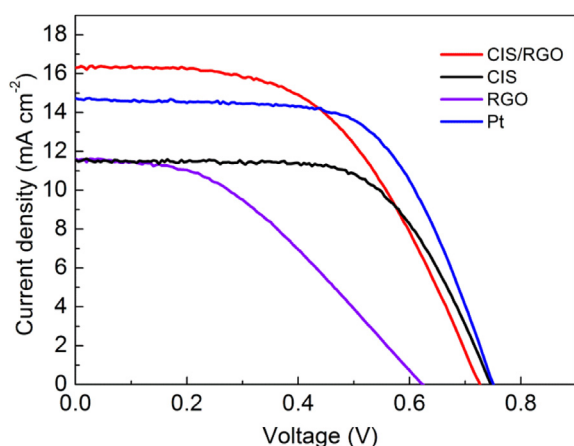


Fig. 5. J-V curves of DSSCs fabricated with various CEs under simulated AM 1.5G solar light (100 mW cm^{-2}).

Table 1
Photovoltaic and electrochemical parameters for different CEs.

	CEs			
	CIS/RGO	CIS	RGO	Pt
V_{oc}/mV	728	745	623	751
$J_{sc}/\text{mA} \cdot \text{cm}^{-2}$	16.61	11.55	11.62	14.77
$FF/\%$	57.56	63.80	38.54	62.39
$PCE/\%$	6.96	5.49	2.79	6.92
R_s/Ω	5.10	9.09	6.15	4.04
R_{ct}/Ω	0.98	4.86	31.00	1.73
$CPE-B/S \cdot s^\beta$	8.24×10^{-6}	3.14×10^{-4}	5.21×10^{-5}	4.02×10^{-5}
$CPE-\beta$	0.99	0.65	0.79	0.90
N_p/Ω	1.38	\	\	\
N_b/Ω	0.84	3.09	\	0.44
$J_0/\text{mA} \cdot \text{cm}^{-2}$	17.88	9.55	4.27	18.05
E_{pp}/V	0.52	0.95	1.27	0.50

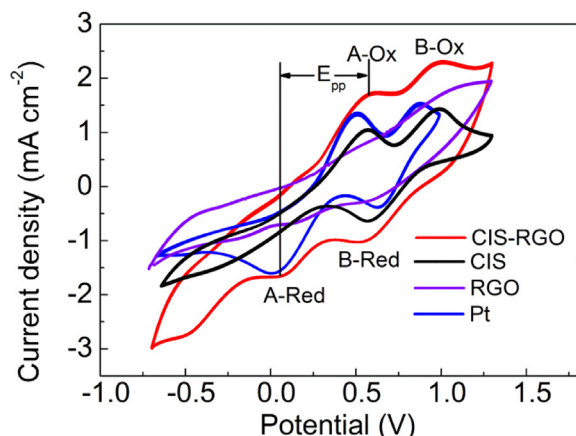


Fig. 6. Cyclic voltammograms of iodide/triiodide redox species of various CES with a measured scan rate of 50 mV s^{-1} (the electrolyte is an acetonitrile solution of 0.1 M LiClO_4 , 10 mM LiI , and 1 mM I_2).

two pairs of oxidation and reduction peaks (A-Ox/A-Red and B-Ox/B-Red) were observed for all CE except RGO CE. Although the exact charge transfer mechanisms are not fully comprehended, previous literatures assign peak A-Ox and A-Red to I^-/I_3^- redox couple and peak B-Ox and B-Red to I_2/I_3^- redox couple, shown in Eq. (1) and Eq. (2), respectively. [16] The peak current and peak-to-peak separation (E_{pp}), as two important parameters, are usually used to evaluate the catalytic activity. Moreover, the E_{pp} is inversely correlated with the standard electrochemical rate constant of a redox reaction, illustrating that a smaller E_{pp} represents a better catalytic activity [52].



The cyclic voltammogram for CIS CE exhibits an obvious A-Ox but a hazy A-Red. However, the cyclic voltammogram for RGO has no evident peaks, illustrating that CIS CE has a better catalytic activity than RGO CE. For the CIS/RGO CE, the cyclic voltammograms are very similar to the Pt CE, indicating that the CIS/RGO CE has a comparable catalytic activity for the redox reaction to Pt CE. In addition, the E_{pp} (as summarized in Table 1) for A-Ox and A-Red of CIS/RGO is smaller than pristine CIS and RGO, illuminating that CIS/RGO CE has a better catalytic activity than each component. This may stems from the positive synergetic effect between the CIS and RGO for reducing I_3^- to I^- , which can vastly improve interfacial charge transfer and increase the number of active catalytic sites. [53] Compared to Pt CE, the E_{pp} is approach to that of Pt revealing an approximate catalytic activity to Pt. Meanwhile, a larger current response is observed for CIS/RGO CE, mainly deriving from the larger roughness. As a plausible cause, it implies that the CIS/RGO CE has high catalytic activity toward the reduction of I_3^- and I_2 [54].

EIS measurements (Fig. 7) were executed on symmetric dummy cells fabricated with two identical CEs (CE/electrolyte/CE), in order to further elucidate the electrocatalytic activity of the as-prepared CEs for the reduction of I_3^- . Obviously, three typical semicircles are observed, which are relevant to the porous structures of materials. [16,55] The intercept on the real axis (Z' -axis) of the high-frequency range is generally assigned to the series resistance (R_s), while the first semicircle is attributed to the charge-transfer resistance (R_{ct} , the radius of the arc on the real axis) and the constant phase element (CPE) at the electrolyte-CE interface. The semicircle in the middle frequency is consistent with the Nernst diffusion impedance (N_p) stemming from the adsorption of iodine

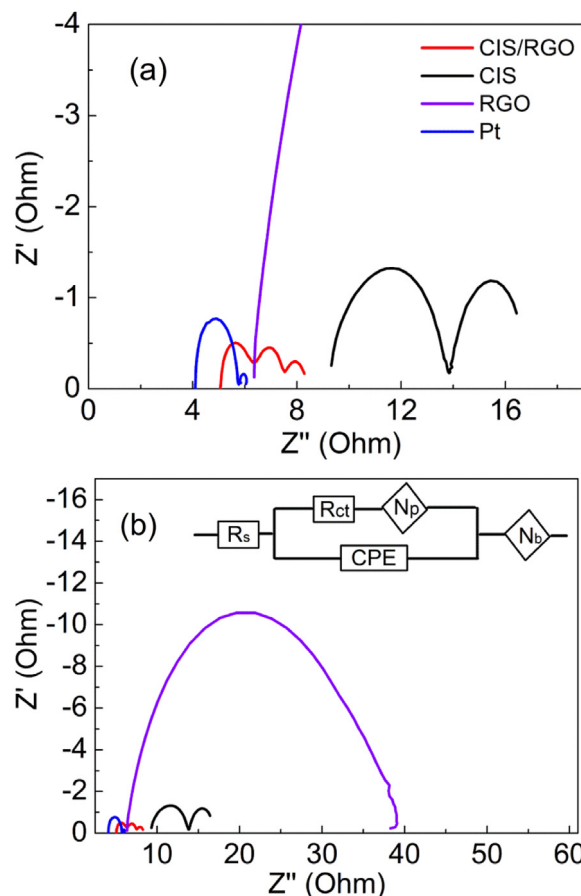


Fig. 7. Nyquist plots of EIS for symmetric cells fabricated with various CEs at (a) reduced and (b) full impedance ranges with the inset of the equivalent circuit diagram.

(I_2)/ I_3^- on the porous electrode surface and the diffusion through the electrode pores. [16,55] The low-frequency semicircle is traditionally determined by bulk Nernst diffusion (N_b) of the I_3^-/I^- redox couple in the electrolyte, and the correlative equivalent circuit were inserted in Fig. 7b. The EIS spectra analysis results are summarized in Table 1 ('-' represents that the data can be omitted due to the related semicircles' disappearance). R_s value of CIS/RGO electrode (5.10Ω) is smaller than pristine CIS (9.09Ω) and RGO (6.15Ω) electrodes, which may attribute to the improvement of the electron transport between FTO glass and the catalytic film due to the introduction of RGO. For RGO, R_s value is larger than that of CIS/RGO which may originate from inferior adhesion between FTO glass and the catalytic film. And the R_s of pristine CIS is even larger than that of RGO, indicating that pristine CIS possesses a relatively inferior conductivity, which is accordance with our research purpose. In general, a smaller R_{ct} represents the higher catalytic activity for the reduction of I_3^- . [21] Distinctly, the closed R_{ct} of CIS/RGO and CIS CEs to Pt CE produce superior catalytic activity towards I_3^- reduction for CIS and its composites. In comparison, R_{ct} of RGO electrode is much larger than the other electrodes, resulting in an inferior catalytic activity. It was generally recognized that a larger CPE represents larger superficial area and roughness, which can improve the catalytic activity. The corresponding impedance of a constant phase element Z_{CPE} can be calculated by Eq. (3), where B and β are frequency independent parameters of CPE ($0 \leq \beta \leq 1$; for $\beta = 1$, the Z_{CPE} transforms into the usual double-layer capacitance). [56] Additionally, smaller Nernst diffusion impedance (N_p and N_b) represent higher transport rate of I^-/I_3^- redox couple in electrolyte,

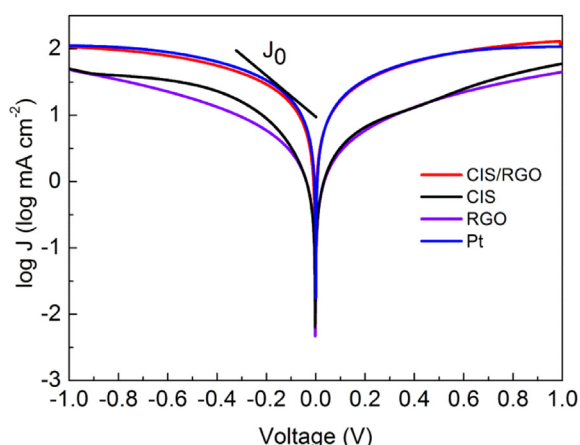


Fig. 8. Tafel polarization curves of various CES that are same as the ones used in EIS measurements.

that is, a larger diffusion coefficient. [11,25] The impedances for CE of different content ratio of GO are summarized in Fig. S2. The impedance of CIS/RGO electrode, by and large, is closed to that of Pt electrode indicating a comparable photovoltaic performance, which was ascertained in Fig. 5.

$$Z_{CPE} = B(I\omega)^{-\beta} \quad (3)$$

Tafel polarization curves were carried out on the symmetrical cells fabricated with different CEs. Fig. 8 shows the logarithmic current density ($\log J$) as a function of voltage (V). Theoretically, the exchange current density (J_0) and the limiting diffusion current density (J_{lim}) which interconnects closely with the catalytic activity of the catalysts can assess the reduction capability of CE materials for I^- and the diffusion capability of I_3^- in electrolyte. The J_0 can be calculated from the intersection of the linear anodic and cathodic curves through Tafel linear extrapolation method. The J_0 of various CEs are increased in the order of RGO (4.27 mA cm^{-2}) < CIS (9.55 mA cm^{-2}) < CIS/RGO (17.88 mA cm^{-2}) \approx Pt (18.05 mA cm^{-2}). In addition, J_0 can be calculated by Eq. (4), where R is the gas constant, T is the absolute temperature, F is Faraday's constant, n is the number of electrons involved in the reduction of I_3^- at the electrode, and R_{ct} is the charge transfer resistance exacted from the EIS spectra (Fig. 5). The J_0 varies inversely with R_{ct} , and R_{ct} is in the order of Pt \approx CIS/RGO < CIS < RGO. Apparently, the variation tendency of J_0 for CIS/RGO, CIS, RGO and Pt CEs obtained in Tafel curves is in well accordance with EIS results. In practical, the steep levels of Tafel polarization curves were used to roughly estimate the catalytic activity of different CE materials. [35] Meanwhile, the Tafel polarization curves for CEs of various content ratio of GO were depicted in Fig. S3.

$$J_0 = \frac{RT}{nFR_{ct}} \quad (4)$$

4. Conclusions

In summary, the CIS/RGO nanocomposites were successfully synthesized via a hydrothermal approach, and higher catalytic performance for reduction I_3^- than pristine CIS and RGO has been obtained on the basis of analysis of CV, EIS and Tafel polarization curves. The PCE for CIS/RGO CE reaches 6.96%, which is comparable to that of Pt CE (6.92%) and significantly higher than that of pristine CIS (5.49%) and RGO CEs (2.79%). The consequence suggests that CIS/RGO is an optional efficient alternative to Pt electrode for DSSCs.

Acknowledgments

This work was financially supported by the State Key Program for Basic Research of China (No. 2013CB632705), National Natural Science Foundation of China (11174002) and by '211 Project' of Anhui University.

Appendix A. Supplementary data

Supplementary data related to this article can be found online at <http://dx.doi.org/10.1016/j.jpowsour.2014.06.172>.

References

- [1] U. Bach, D. Lupo, P. Comte, J. Moser, F. Weissörtel, J. Salbeck, H. Spreitzer, M. Grätzel, *Nature* 395 (1998) 583–585.
- [2] M. Grätzel, *Nature* 414 (2001) 338–344.
- [3] M.K. Nazeeruddin, P. Pechy, T. Renouard, S.M. Zakeeruddin, R. Humphry-Baker, P. Comte, P. Liska, L. Cevey, E. Costa, V. Shklover, *J. Am. Chem. Soc.* 123 (2001) 1613–1624.
- [4] M.K. Nazeeruddin, F. De Angelis, S. Fantacci, A. Selloni, G. Viscardi, P. Liska, S. Ito, B. Takeru, M. Grätzel, *J. Am. Chem. Soc.* 127 (2005) 16835–16847.
- [5] T. Bessho, S.M. Zakeeruddin, C.Y. Yeh, E.W.G. Diau, M. Grätzel, *Angew. Chem. Int. Ed.* 49 (2010) 6646–6649.
- [6] F. Sauvage, J.D. Decoppet, M. Zhang, S.M. Zakeeruddin, P. Comte, M. Nazeeruddin, P. Wang, M. Grätzel, *J. Am. Chem. Soc.* 133 (2011) 9304–9310.
- [7] A. Yella, H.W. Lee, H.N. Tsao, C. Yi, A.K. Chandiran, M.K. Nazeeruddin, E.W.G. Diau, C.Y. Yeh, S.M. Zakeeruddin, M. Grätzel, *Science* 334 (2011) 629–634.
- [8] J. Burschka, N. Pellet, S.J. Moon, R.H. Baker, P. Gao, M.K. Nazeeruddin, M. Grätzel, *Nature* 499 (2013) 316–319.
- [9] M. Liu, M.B. Johnston, H.J. Snaith, *Nature* 501 (2013) 395–398.
- [10] S. Mathew, A. Yella, P. Gao, R.H. Baker, B.F.E. Curchod, N.A. Astani, I. Tavernelli, U. Rothlisberger, M.K. Nazeeruddin, M. Grätzel, *Nat. Chem.* 6 (2014) 242–247.
- [11] A. Hauch, A. Georg, *Electrochim. Acta* 46 (2001) 3457–3466.
- [12] J.H. Wu, Z.Y. Tang, Y.F. Huang, M.L. Huang, H.J. Yu, J.M. Lin, *J. Power Sources* 257 (2014) 84–89.
- [13] J. Xia, N. Masaki, K. Jiang, S. Yanagida, *J. Mater. Chem.* 17 (2007) 2845–2850.
- [14] R. Trevisan, M. Döbelin, P.P. Boix, E.M. Barea, R. Tena-Zaera, I. Mora-Seró, J. Bisquert, *Adv. Energy. Mater.* 1 (2011) 781–784.
- [15] B.L. He, Q.W. Tang, M. Wang, C.Q. Ma, S.S. Yuan, *J. Power. Sources* 256 (2014) 8–13.
- [16] J.D. Roy-Mayhew, D.J. Bozym, C. Punckt, I.A. Aksay, *ACS Nano* 4 (2010) 6203–6211.
- [17] C. Luo, X. Zuo, L. Wang, E. Wang, S. Song, J. Wang, J. Wang, C. Fan, Y. Cao, *Nano Lett.* 8 (2008) 4454–4458.
- [18] P. Joshi, L. Zhang, Q. Chen, D. Galipeau, H. Fong, Q. Qiao, *ACS Appl. Mater. Inter.* 2 (2010) 3572–3577.
- [19] K.T. Demele, R. Nechache, L. Nikolova, A. Vomiero, C. Santato, S. Licoccia, F. Rosei, *J. Power Sources* 233 (2013) 93–97.
- [20] D. Sebastián, V. Baglio, M. Girolamo, R. Moliner, M. Lázaro, A. Aricò, *J. Power Sources* 250 (2014) 242–249.
- [21] M. Wu, X. Lin, A. Hagfeldt, T. Ma, *Angew. Chem. Int. Ed.* 50 (2011) 3520–3524.
- [22] M. Wang, A.M. Anghel, B.t. Marsan, N.L. Cevey, N. Pootrakulchote, S.M. Zakeeruddin, M. Grätzel, *J. Am. Chem. Soc.* 131 (2009) 15976–15977.
- [23] Q. Jiang, G. Li, S. Liu, X. Gao, *J. Phys. Chem. C* 114 (2010) 13397–13401.
- [24] W.S. Chi, J.W. Han, S. Yang, D.K. Roh, H. Lee, J.H. Kim, *Chem. Commun.* 48 (2012) 9501–9503.
- [25] M. Wu, X. Lin, A. Hagfeldt, T. Ma, *Chem. Commun.* 47 (2011) 4535–4537.
- [26] F. Gong, H. Wang, X. Xu, G. Zhou, Z.S. Wang, *J. Am. Chem. Soc.* 134 (2012) 10953–10958.
- [27] Z. Wen, S. Cui, H. Pu, S. Mao, K. Yu, X. Feng, J. Chen, *Adv. Mater.* 23 (2011) 5445–5450.
- [28] J.Y. Lin, J.H. Liao, T.Y. Hung, *Electrochem. Commun.* 13 (2011) 977–980.
- [29] W. Zhao, T. Lin, S. Sun, H. Bi, P. Chen, D. Wan, F. Huang, *J. Mater. Chem. A* 1 (2013) 194–198.
- [30] H.K. Mulmudi, S.K. Batabyal, M. Rao, R.R. Prabhakar, N. Mathews, Y.M. Lam, S.G. Mhaisalkar, *Phys. Chem. Chem. Phys.* 13 (2011) 19307–19309.
- [31] X. Xin, M. He, W. Han, J. Jung, Z. Lin, *Angew. Chem. Int. Ed.* 50 (2011) 11739–11742.
- [32] J.L. Shay, J.H. Wernick, *Ternary Chalcopyrite Semiconductors: Growth, Electronic Properties and Applications*, first ed., Pergamon, New York, 1975.
- [33] K. Ernst, A. Belaidi, R. Könenkamp, *Semicond. Sci. Tech.* 18 (2003) 475.
- [34] S.W. Wang, Y.H. Zhu, X.L. Yang, C.Z. Li, *Electroanalysis* 26 (2014) 573–580.
- [35] Z. Li, F. Gong, G. Zhou, Z.S. Wang, *J. Phys. Chem. C* 117 (2013) 6561–6566.
- [36] Y. Zhu, S. Murali, W. Cai, X. Li, J.W. Suk, J.R. Potts, R.S. Ruoff, *Adv. Mater.* 22 (2010) 3906–3924.
- [37] D.C. Marcano, D.V. Kosynkin, J.M. Berlin, A. Sinitskii, Z. Sun, A. Slesarev, L.B. Alemany, W. Lu, J.M. Tour, *ACS Nano* 4 (2010) 4806–4814.

- [38] S. Chen, J. Zhu, X. Wu, Q. Han, X. Wang, *ACS Nano* 4 (2010) 2822–2830.
- [39] H.P. Cong, J.J. He, Y. Lu, S.H. Yu, *Small* 6 (2010) 169–173.
- [40] J. Shen, Y. Hu, M. Shi, X. Lu, C. Qin, C. Li, M. Ye, *Chem. Mater.* 21 (2009) 3514–3520.
- [41] H. Wang, Y. Liang, Y. Li, H. Dai, *Angew. Chem. Int. Ed.* 50 (2011) 10969–10972.
- [42] J.A. Garcia, A.P. Rodriguez, A.R. Rodriguez, T. Jawhari, J. Morante, R. Scheer, W. Calvet, *Thin Solid Films* 387 (2001) 216–218.
- [43] E. Rudigier, I. Luck, R. Scheer, *Appl. Phys. Lett.* 82 (2003) 4370–4372.
- [44] J. Álvarez-García, J. Marcos-Ruzafa, A. Pérez-Rodríguez, A. Romano-Rodríguez, J. Morante, R. Scheer, *Thin Solid Films* 361 (2000) 208–212.
- [45] F. Tuinstra, J.L. Koenig, *J. Chem. Phys.* 53 (1970) 1126.
- [46] Y.W. Zhang, J.Q. Tian, H.Y. Li, L. Wang, X.Y. Qin, A.M. Asiri, A.O.A. Youbi, X.P. Sun, *Langmuir* 28 (2012) 12893–12900.
- [47] S. Stankovich, D.A. Dikin, R.D. Piner, K.A. Kohlhaas, A. Kleinhammes, Y. Jia, Y. Wu, S.T. Nguyen, R.S. Ruoff, *Carbon* 45 (2007) 1558–1565.
- [48] D. Chen, X. Zhao, S.S. Chen, H.F. Li, X.N. Fu, Q.Z. Wu, S.P. Li, Y. Li, B.L. Su, *Carbon* 68 (2014) 755–762.
- [49] S. Pan, X. Liu, *J. Solid. State. Chem.* 191 (2012) 51–56.
- [50] G.D. Nie, L. Zhang, X.F. Lu, X.J. Bian, W.N. Sun, C. Wang, *Dalton Trans.* 42 (2013) 14006–14013.
- [51] F.M. Ye, G.H. Du, Z.F. Jiang, Y.J. Zhong, X.D. Wang, Q.P. Cao, J.Z. Jiang, *Nanoscale* 4 (2012) 7354–7357.
- [52] R.Y. Yao, Z.J. Zhou, Z.L. Hou, X. Wang, W.H. Zhou, S.X. Wu, *ACS Appl. Mater. Inter.* 5 (2013) 3143–3148.
- [53] Q. Xiang, J. Yu, M. Jaroniec, *J. Am. Chem. Soc.* 134 (2012) 6575–6578.
- [54] S.J. Yuan, Z.J. Zhou, Z.L. Hou, W.H. Zhou, R.Y. Yao, Y. Zhao, S.X. Wu, *Chem.-Eur. J.* 31 (2013) 10107–10110.
- [55] H. Xu, X. Zhang, C. Zhang, Z. Liu, X. Zhou, S. Pang, X. Chen, S. Dong, Z. Zhang, L. Zhang, *ACS Appl. Mater. Inter.* 4 (2012) 1087–1092.
- [56] L. Kavan, J.H. Yum, M. Grätzel, *ACS Nano* 5 (2010) 165–172.